

CO Distribution and Kinematics Along the Bar in the Strongly Barred Spiral NGC 7479

S. Laine

*Department of Physical Sciences, University of
Hertfordshire, College Lane, Hatfield, AL10 9AB, United
Kingdom, seppo@star.herts.ac.uk*

J. D. P. Kenney

*Astronomy Department, Yale University, P.O. Box
208101, New Haven, CT 06520-8101,
kenney@astro.yale.edu*

M. S. Yun

*National Radio Astronomy Observatory, 1003 Lopezville
Road, Socorro, NM 87801-0387, myun@nrao.edu*

and

S. T. Gottesman

*Department of Astronomy, P.O. Box 112055, University
of Florida, Gainesville, FL 32611-2055,
gott@astro.ufl.edu*

Abstract

We report on the $2''.5$ (400 pc) resolution CO ($J = 1 \rightarrow 0$) observations covering the whole length of the bar in the strongly barred late-type spiral galaxy NGC 7479. CO emission is detected only along a dust lane that traverses the whole length of the bar, including the nucleus. The emission is strongest in the nucleus. The distribution of emission is clumpy along the bar outside the nucleus, and consists of gas complexes that are unlikely to be gravitationally bound. The CO kinematics within the bar consist of two separate components. A kinematically distinct circumnuclear disk, < 500 pc in diameter, is undergoing predominantly circular motion with a maximum rotational velocity of 245 km s^{-1} at a radius of $1''$ (160 pc). The CO-emitting gas in the bar outside the circumnuclear disk has substantial noncircular motions which are consistent with a large radial velocity component, directed inwards. The CO emission has a large velocity gradient across the bar dust lane, ranging from 0.5 to $1.9 \text{ km s}^{-1} \text{ pc}^{-1}$ after correcting for inclination and the projected velocity change across the dust lane is as high as 200 km s^{-1} . This sharp velocity gradient is consistent with a shock front at the location of the bar dust lane. A comparison of $\text{H}\alpha$ and CO kinematics across the dust lane shows that although the $\text{H}\alpha$ emission is often observed both upstream and downstream from the dust lane, the CO emission is observed only where the velocity gradient is large. We also compare the observations with hydrodynamic models and discuss star formation along the bar.

Subject headings: galaxies: evolution — galaxies: individual (NGC 7479) — galaxies: ISM — galaxies: kinematics

and dynamics — galaxies: starburst — galaxies: structure

1. Introduction

To investigate the various factors that determine the molecular gas morphology and kinematics in the bars of spiral galaxies we need to obtain observations of galaxies which have molecular gas in both the nucleus and the bar. NGC 7479 is one of the few galaxies which have abundant molecular gas along most of the bar and in the nucleus (Quillen et al. 1995). It is an isolated, large, strongly barred SBc galaxy at a moderate distance (32 Mpc, assuming $H_0 = 75 \text{ km s}^{-1}$, a heliocentric velocity of $V = 2371 \text{ km s}^{-1}$ and no correction for the local group velocities; $1'' = 160 \text{ pc}$). It has both abundant atomic gas (Laine & Gottesman 1998) and molecular gas (Young & Devereux 1991), and it has been classified as a starburst galaxy based on its large and centrally concentrated $10 \mu\text{m}$ flux (Devereux 1989).

We have obtained new, high resolution (synthesized beam = $2''.7 \times 2''.1$, position angle = -85°) 2.6 mm CO ($J = 1 \rightarrow 0$) observations of NGC 7479, and investigate the gas kinematics and distribution in the unusually gas-rich bar. We have detected a strong central molecular gas component and weaker emission along the bar, closely following the leading dust lane, as previously shown by the lower resolution ($7''$) CO maps (Quillen et al. 1995). Our new data have greater sensitivity and spatial resolution. The emphasis in this paper is on the interesting CO kinematics in both the nuclear area and in the offset gas/dust lane along the bar. Other papers in this series address the distribution and kinematics of the neutral, atomic hydrogen gas in NGC 7479 (Laine & Gottesman 1998), the stellar bar pattern speed of NGC 7479 (Laine, Shlosman, & Heller 1998), and the minor merger model for NGC 7479 (Laine & Heller 1998).

2. Observations

The new CO observations were made at the Owens Valley Radio Observatory (OVRO) Millimeter Array.¹ NGC 7479 was observed in three different configurations of the array. The observations were made on 1994 October 7, November 23–24, and 1995 January 18–19. The total integration times at each of the three observed positions and other observing parameters are given in Table 1. The total single sideband temperatures, including the effects of the atmosphere, were typically 350 – 500 K . Variations in the sky opacity and receiver gain were corrected through measure-

¹The Owens Valley Radio Observatory Millimeter array is operated by the California Institute of Technology with support from the National Science Foundation.

ments of an ambient temperature chopper wheel. The pointing was checked at the beginning of each track, and the strong quasar 3C 454.3 was observed every 19 minutes to serve as a bandpass and gain calibrator, as well as a secondary flux calibrator.

The calibration followed standard procedures. After correcting for the atmospheric and instrumental gain variations, we produced channel and integrated maps of the CO emission. For mapping the visibility data, natural weighting was used to achieve the highest sensitivity. We used 15 mJy beam⁻¹ (1.5σ) as the stopping criterion for the CLEAN iterations. The map parameters are given in Table 2. We combined the three observed positions into a mosaic image, correcting for the attenuation of the primary beam. The velocity-smoothed channel maps of the CO emission are shown in Figure 1. The measured line of sight CO velocities quoted in this paper are with respect to the LSR unless otherwise stated. The mapped regions have been drawn with great circles in Figure 2, which shows the integrated flux map.

We also present data from Hα Fabry–Perot observations, kindly given to us by Drs. Stuart Vogel and Michael Regan. These observations were made with the Maryland–Caltech Fabry–Perot Spectrometer (see, e.g. Vogel et al. 1995) attached to the Cassegrain focus of the 1.5 m telescope at Palomar Observatory. The data were obtained on 1994 September 29–30. 40 exposures were taken, each with a 500 second integration time and a pixel scale of 1''.88 pixel⁻¹. To improve the signal to noise ratio, these data have been smoothed to 3''.6 spatial resolution. The velocity planes are separated by 12.1 km s⁻¹. The velocity uncertainty (rms) is estimated as 1–2 km s⁻¹. The data reduction procedure followed that of Regan et al. (1996), who give a more detailed description.

3. Results

3.1. CO Flux and Distribution

The integrated ¹²CO (1–0) flux map of the whole mapped area and the mean velocity field of the central gas complex are displayed in Figures 2 and 3, respectively. The unit of the integrated flux map has been converted to $N(\text{H}_2)$ cm⁻² with the “standard conversion factor” (Bloemen et al. 1986; Scoville et al. 1987; Kenney & Young 1989),

$$N(\text{H}_2) \text{ cm}^{-2} = 3.0 \times 10^{20} \int T_{\text{B}}(\text{CO}) dv \text{ K km s}^{-1}. \quad (1)$$

The CO flux spectrum is plotted in Figure 4. The total integrated flux is 266±40 Jy km s⁻¹, where the stated uncertainty is the rms value in the measured fluxes. In addition, systematic uncertainties in the

flux of the secondary calibrator (15%) can lead to a systematic over- or underestimation of the fluxes. For comparison, the total, integrated single dish CO flux for the whole galaxy (4'×3') is 1050±200 Jy km s⁻¹ (Young et al. 1995), but for the central 45'' only, we estimate a CO flux of 430±65 Jy km s⁻¹ (Kenney 1996).

At least 62% ± 20% of the flux in the central zone of the galaxy has been detected by our high resolution OVRO interferometer observations. Our interferometer observations have some sensitivity to structures up to 50'' in size, although the sensitivity starts to decrease for structures with sizes larger than half the field of view (structures with sizes > 30''). The “missing” flux could be associated with large scale structures (> 30'') for which our interferometer measurements are not fully sensitive. However, it is unlikely that a single velocity channel (width = 10 km s⁻¹) would have continuous CO emission structures this large. More likely, our brightness temperature sensitivity (rms = 0.2 K, corresponding to an H₂ column density of about 10²² molecules cm⁻² averaged over the beam, using the standard conversion factor) is not good enough to detect the emission from regions with low beam-averaged CO surface densities. We will keep these limitations in mind when discussing the implications of our observations in § 4.

Fig. 2 reveals that all the detected CO emission comes from a nearly linear ridge which is offset towards the leading edges of the bar (assuming the spiral arms are trailing). This ridge has a full-width-half-maximum (FWHM) value similar to the width of the beam (2''.7), indicating that the gas/dust lane is unresolved. The dust lane, as measured from 0''.8 resolution optical and near-infrared images, has a width of about 1''.5. Therefore, the high density molecular gas ridge does not have a width larger than that of the dust lane. The CO emission intensity has a strong peak in the nucleus, but overall the emission crosses the nucleus smoothly along position angle (PA) –10°, connecting the two linear, offset parts of the bar gas/dust ridge.

Applying the standard CO-to-H₂ conversion factor and multiplying the resulting masses by 1.35 to account for helium, the molecular mass within the central 1'' (160 pc) radius is 3.3 × 10⁸ M_⊙ and the mean gas mass surface density in this area is 4.1 × 10³ M_⊙ pc⁻². This should be compared with the galactic center molecular gas mass of 3 × 10⁷ M_⊙ within the central 500 pc (Dahmen et al. 1998) that has an average molecular gas surface density of 150 M_⊙ pc⁻². The corresponding hydrogen column density in the nucleus of NGC 7479 is about 1.6 × 10²³ cm⁻² which implies a beam-smoothed optical extinction (A_V) value of almost a hundred magnitudes. Extinction will be further discussed when

Table 1: Observing parameters at OVRO.

Parameter	Value
Pointing center 1	R.A. 23 ^h 02 ^m 25 ^s .99 Dec. 12° 02' 24''.2
Pointing center 2	R.A. 23 ^h 02 ^m 26 ^s .30 Dec. 12° 03' 09''.0
Pointing center 3	R.A. 23 ^h 02 ^m 26 ^s .61 Dec. 12° 03' 53''.7
Central frequency	114.37 GHz
Central velocity (LSR)	2340 km s ⁻¹
Configurations used	A, B, C
Total number of antennas	A=5, B=6, C=6
Field of view	63''
Spatial scales sampled ^a	2''.5 – 50''
Baseline lengths	4.0 – 92.7 kλ
Integration time (min), p.c. 1	350
p.c. 2	360
p.c. 3	360
Absolute flux calibrator	Neptune, $T_B = 114$ K
Secondary flux calibrator	3C454.3
Velocity resolution	10.4 km s ⁻¹
Total observed bandwidth	464 MHz = 1206.4 km s ⁻¹

^aSee text in § 3.1 for more information.

Table 2: Parameters of the ¹²CO channel maps.

Parameter	Value
Size of synthesized beam	2''.7 × 2''.1
Size of beam in parsecs ^a	262 × 204
PA of synthesized beam	-85°
Weighting used to make maps	Natural
Rms noise in channel maps	0.011 Jy beam ⁻¹ =0.19 K
Theor. rms noise in channel maps	0.0115 Jy beam ⁻¹ =0.20 K
Peak brightness temperature	3.83 K
Radio continuum flux density ^b	< 4 mJy

^aAssuming a distance of 32 Mpc.

^bA 5σ upper limit is given for a point source.

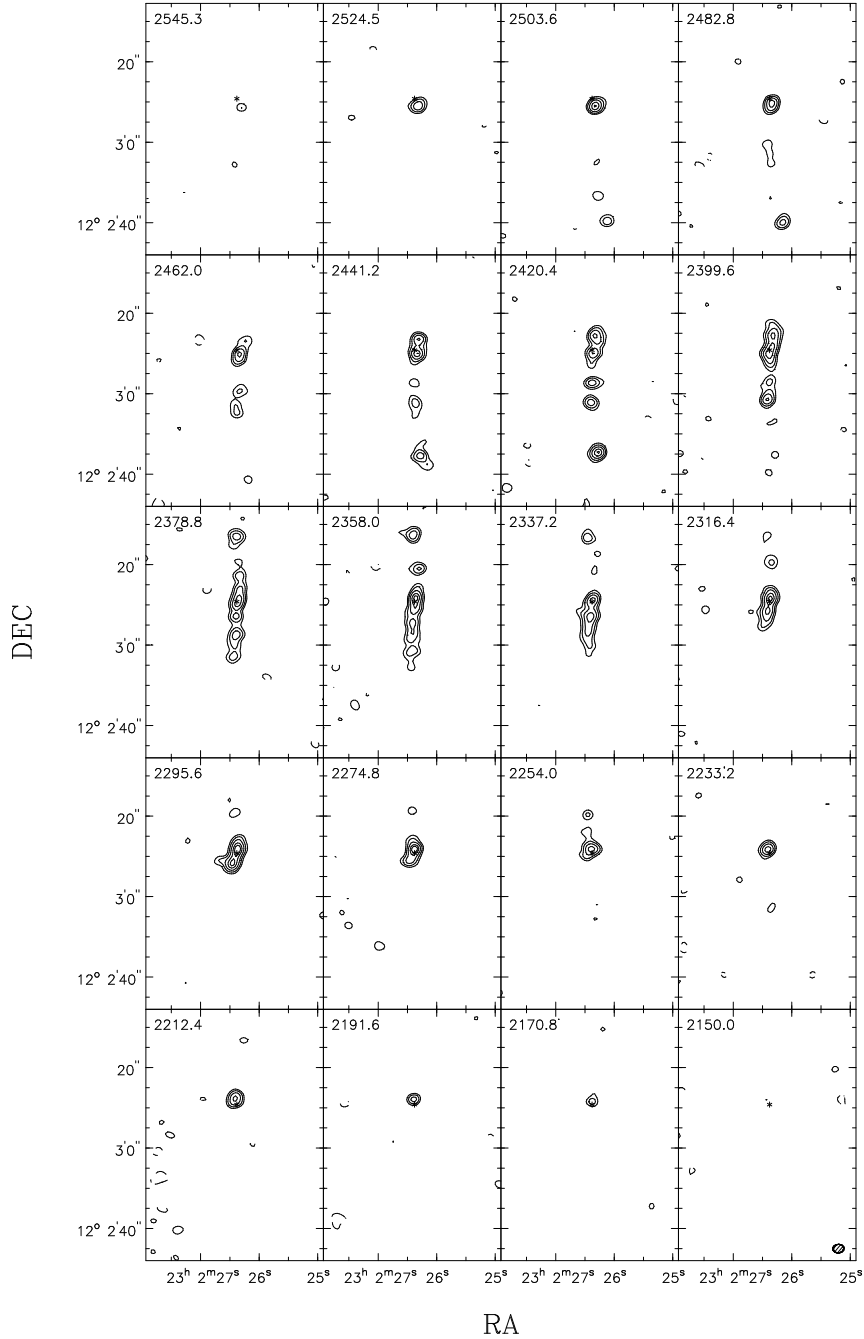


Fig. 1.— The 20 km s^{-1} channel maps of the naturally weighted CO cube. The contour levels are at $(-3, 3, 5, 8, 12, 15) \times 0.021 \text{ Jy/beam}$. The star marks the K -band nucleus. The velocity at the center of each channel is given in the upper left of each frame and the beam (2.7×2.1) at the bottom right of the last frame. Note the strong emission near the nucleus in most of the channels, due to the circularly rotating circumnuclear disk.

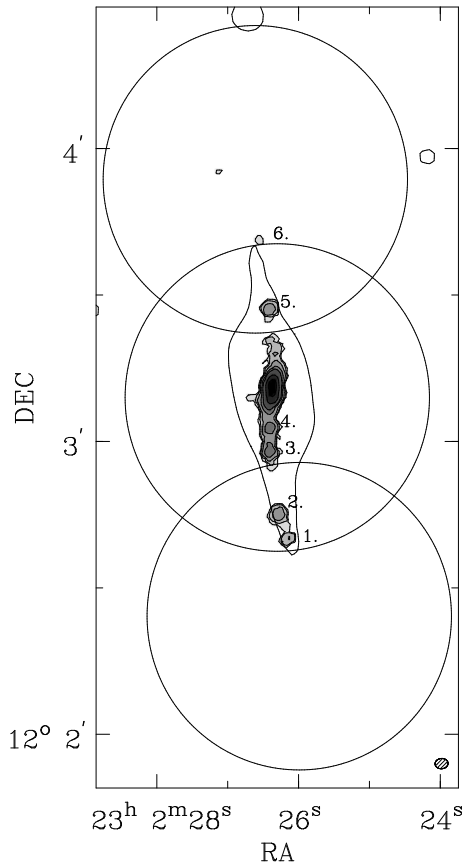


Fig. 2.— The naturally weighted integrated map of $^{12}\text{CO}(1-0)$ emission. The contour and gray scale levels are $(4, 8, 16, 32, 48, 96, 144) \times 10^{21} \text{ H}_2 \text{ molecules cm}^{-2}$. The contour around the CO emission is the 17.1 mag arcsec $^{-2}$ level of a K -band image (Quillen et al. 1995), showing the location of the stellar bar. The PA of the stellar bar and that of the gaseous bar are different, since the gas is in a leading dust lane. The beam is shown at the bottom right corner of the map. The main CO clumps have been numbered. The beams around the three observed positions have been drawn with large circles.

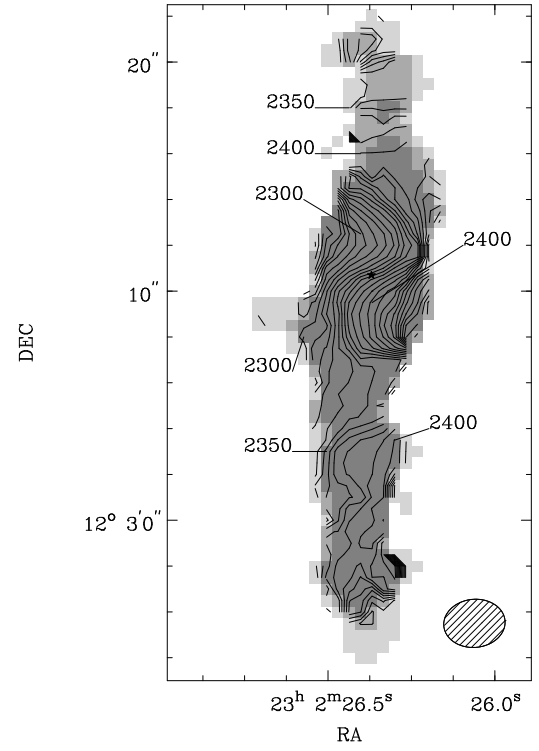


Fig. 3.— A magnified image of the central CO velocity field superposed on the integrated CO emission map. The CO emission peak is marked with a star in the nucleus. The gray scale levels have been chosen to show only the brightest CO emission. The isovelocity contours in this map do not accurately reflect the interesting gas kinematics in some regions. The Z-shaped contours near the center occur where the inwardly flowing bar gas meets the kinematically distinct circumnuclear disk. These two distinct components are better displayed in Fig. 7. The large velocity gradient across the bar dust lane, which we have marginally resolved, is better displayed in Fig. 8.

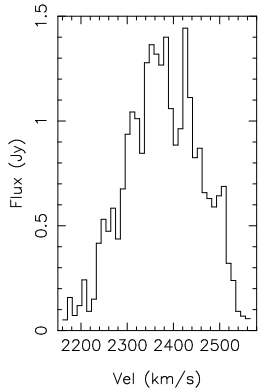


Fig. 4.— The spectrum of the CO emission detected with the OVRO millimeter interferometer. The channel fluxes have uncertainties of the order of 5%.

addressing the star formation rates in § 4.2. The molecular gas mass in the central $7''$ diameter region is about $2 \times 10^9 M_{\odot}$ and the total molecular mass derived from our observations is $4 \times 10^9 M_{\odot}$. Roughly half ($2 \times 10^9 M_{\odot}$) of the detected flux (and mass) lies along the bar outside the central $7''$ diameter region.

The detected CO emission along the bar is highly clumpy. In the integrated flux map (Fig. 2) at least six separate clumps in addition to the nuclear gas complex can be identified. The masses of the clumps along the bar range from $9 \times 10^6 M_{\odot}$ to $2 \times 10^8 M_{\odot}$. However, the use of the standard CO-to-H₂ conversion factor may not be justified in strongly shocked gas along the bar. The temperature and density are likely to be higher in the shock, although these effects tend to offset each other. If the clouds in the shock are not gravitationally bound (see § 4.1.2) their large line widths cause the standard CO-to-H₂ conversion to overestimate the H₂ mass. Shock chemistry can also change the conversion factor. The lower limit for the conversion factor is obtained for optically thin CO emission which has a conversion factor 20 times smaller than the standard factor (cf. Bryant & Scoville 1996). Overall, it is difficult to ascertain how the conversion factor would change in bar shocks.

The sizes of the clumps along the bar are too large to be individual self-gravitating giant molecular clouds but their sizes and masses are similar to those of giant molecular associations (GMAs) found in the nearby spiral galaxies M 51, M 100 (Rand 1993a, 1993b, 1995), and NGC 4414 (Sakamoto 1996). However, the clumps in NGC 7479 are kinematically very different from those observed in the other galaxies (§ 4.1.2).

The azimuthally averaged radial profile of the molecular gas is compared to the radial profiles of *R*- and *K*-band light, H α , H I, and $\lambda = 21$ cm radio continuum emission in Figure 5. The optical and near-infrared images were first smoothed to the spatial resolution of our CO data ($2''.5$). However, the radio continuum and the H I data (from Laine & Gottesman 1998) have resolutions of $4''$ and $15''$, respectively.

Within the central $7''$ the CO emission intensity rises by more than an order of magnitude, as in NGC 3504 (Kenney, Carlstrom, & Young 1993). Unlike NGC 3504, the *R*- and *K*-band profiles are shallower than the CO profile in this area. This may reflect the lack of an intense starburst in the nucleus of NGC 7479, its relatively small bulge component or large extinction. The CO to H α intensity ratio is approximately constant in the central $2''$, where the nuclear gas disk lies, as in NGC 3504 (Kenney et al. 1993). Outside this inner region NGC 3504 and NGC 7479 show opposite behaviours: in NGC 3504 the H α gradient becomes steeper than the CO intensity profile, whereas in NGC 7479 the opposite is true.

This could mean that the star formation efficiency increases outwards from the center in NGC 7479. Unfortunately, there are no suitable radio continuum measurements which would allow us to assess the effects of extinction. In other galaxies comparisons between the 6 cm thermal emission and H α have shown that extinction can change the “picture” (e.g. M 100; García-Burillo et al. 1998).

The radio continuum emission is very strongly peaked in the nucleus. These data are shown at $4''$ resolution, so the gradient at a higher resolution is likely to be even larger. If the radio continuum is regarded as a star formation tracer, the star formation efficiency decreases with radius as in NGC 3504. However, the nucleus of NGC 7479 is slightly active (LINER), and the radio continuum may also have a contribution from the nucleus, not related to star formation.

Figure 5*b* shows the striking difference in the distribution of H I and CO emissions. It should be noted that our CO observations did not extend very far out into the spiral arms of NGC 7479. The atomic gas appears to have been converted into the molecular form at the higher pressures of the central potential well, aided by the self-gravity of the gas.

3.2. Gas motions

The line of sight velocity field (Fig. 3) is complex and difficult to interpret. The contours in the nuclear few arcsec region are aligned perpendicular to the PA of the outer disk (22° ; Laine & Gottesman 1998), consistent with solid body rotation. Beyond $3''$ radius in the south, the line of sight velocity contours are aligned roughly along the bar. This morphology of the velocity field is consistent with a large radial velocity component (along the bar; e.g., Lindblad et al. 1996). The northern part of the bar does not have a sufficiently extended emission region in which we could estimate the character of the gas motion.

The central $4''$ region of the velocity field where the circularly rotating gas and the gas flowing along the bar meet has a Z-shape. To better understand the gas motions in the bar we have made position-velocity plots at several different PAs and spatial locations.

Position-velocity plots close to the major axis (at PA 25°) and along the bar are presented in Figures 6 and 7, respectively. Both plots are centered at the nuclear CO emission peak (R.A. $23^{\text{h}} 02^{\text{m}} 26^{\text{s}}.37$, Dec. $12^\circ 03' 11''.1$; B1950.0) as determined from the map of integrated CO emission (Fig. 2), and represent planes (width $0''.5$) of the original data cube. Outside the central $2''$ region, the mean CO velocity within each emission region along the bar does not deviate from the mean velocity (2360 km s^{-1}) of the nuclear region by more than 50 km s^{-1} (Fig. 7). Fig. 7 also has a line which indicates the location where emission would

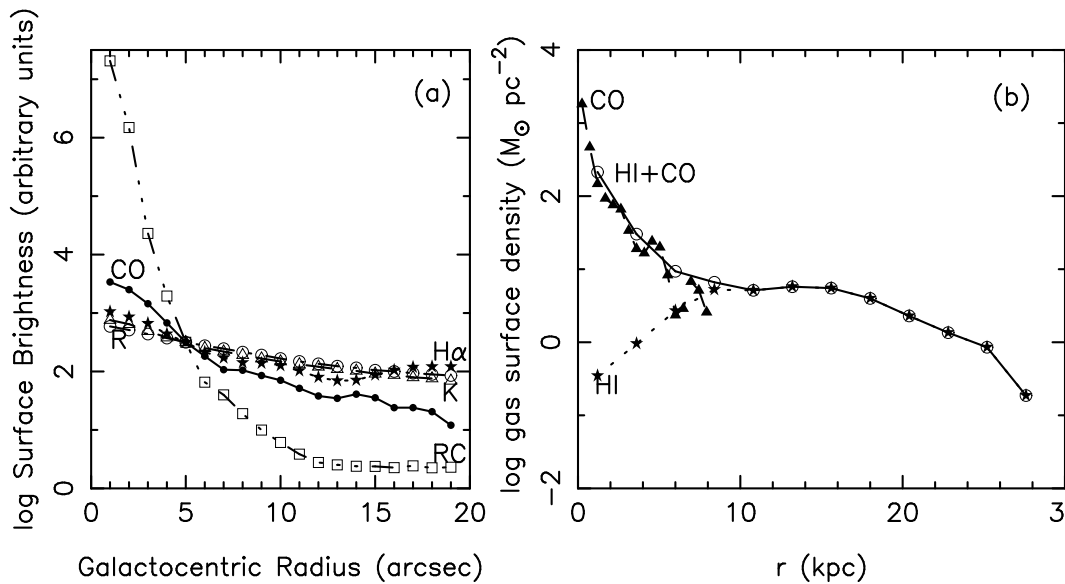


Fig. 5.— (a). The azimuthally averaged radial profiles of the CO emission, H α emission, R -band and K -band light, and $\lambda = 21$ cm radio continuum (RC) in the central area of NGC 7479. The data have been smoothed to the same spatial resolution of $2''.5$, except the radio continuum ($4''$). For the CO, the vertical axis gives the total molecular mass surface density in $M_{\odot} \text{ pc}^{-2}$, calculated using the standard CO-H $_2$ conversion factor. The other profiles, which have arbitrary units, have been normalized to agree at $5.0''$. The H α data are from Young & Devereux (1991), the R -band data were kindly provided by P. Martin and D. Friedli, taken at the Steward Observatory 2.3 m telescope on Kitt Peak. The K -band data are from Quillen et al. (1995). The 21 cm radio continuum is from Laine & Gottesman (1998). (b) Azimuthally averaged radial profiles of the CO ($2''.5$ spatial resolution) and H I ($15''$ spatial resolution) emission in NGC 7479, together with the total (molecular + neutral hydrogen) gas profile. The vertical scale gives the mass surface density in $M_{\odot} \text{ pc}^{-2}$. The molecular profile is shown with filled triangles, connected with dashes, the H I profile with stars, connected with dots, and the total gas (molecular + neutral hydrogen) profile with open circles, connected with a solid line.

be expected if it followed the rotation curve derived from the gravitational potential, obtained by converting the K -band surface brightness into a mass surface density (Quillen et al. 1995). Since Quillen et al. (1995) did not consider the three-dimensional nature of the bulge, and the M/L ratio as determined from a K -band image may be variable near the nucleus, the gravitational potential and the rotation curve in the central $8''$ are uncertain.

The remarkable departures of the observed emission from the expected location traced by the line in Fig. 7 outside the nuclear region indicate that the gas motion along the bar is inconsistent with pure circular rotation. Assuming that the northwestern side of the galaxy is the near side (spiral arms trailing) and that there are no substantial vertical motions, it is possible to make a rough estimate of the radial velocity of the gas along the bar, taking the tangential speed of the gas in the bar from the bar rotation rate. There will be an additional component of tangential speed, but if the gas is captured in orbits that are elongated along the bar, a first order estimate of the tangential velocity is provided by the bar pattern speed. Using the bar pattern speed of $27 \text{ km s}^{-1} \text{ kpc}^{-1}$ (Laine et al. 1998), the tangential velocity at the distance of $15''$ (3.2 kpc) is 65 km s^{-1} . The observed velocity at this point in the clump north of the center is only slightly higher, 2370 km s^{-1} , than the velocity of the nucleus. Accounting for the difference between the directions of the gas bar major axis and the line of nodes (about 31°) and the inclination (51° ; Laine & Gottesman 1998), the observed emission velocities can be reproduced with a radial inflow component of 110 km s^{-1} .

The plot along the CO major axis (Figure 6a) also gives a hint of the existence of two separate kinematic components. The first component shows up as a large linear velocity gradient across the central few arc seconds ($190 \text{ km s}^{-1} \text{ arcsec}^{-1}$ or $1.2 \text{ km s}^{-1} \text{ pc}^{-1}$) that is consistent with solid body rotation. After correcting the observed velocities for the inclination, the maximum rotation velocity in the nuclear disk is 245 km s^{-1} at a radius of $1''$. The noncircular kinematic component can be seen as extensions toward lower declinations and lower velocities (marked with E1 in Fig. 6a) and higher declinations and higher velocities (marked with E2 in Fig. 6a).

We have also made position-velocity maps perpendicular to the bar (at PA 90°) at several positions along the bar, using both the CO and the $\text{H}\alpha$ data cubes. The resulting maps, together with an image of the integrated CO and $\text{H}\alpha$ emissions, are shown in Figure 8. The fluxes between the horizontal boundaries indicated in the map were summed together to improve the signal-to-noise ratios within every numbered region. The velocity resolutions are 10.4 km s^{-1}

(CO) and 12.1 km s^{-1} ($\text{H}\alpha$).

The overlay of the total CO intensity (at $2''.5$ spatial resolution) contours on an $\text{H}\alpha$ image (at $0''.8$ spatial resolution, kindly given to us by Dr. J. Knapen) reveals that the CO and $\text{H}\alpha$ emission peaks occur mostly at the same locations within the available spatial resolution. However, in regions 3 and 7, the $\text{H}\alpha$ emission maxima are at a larger radius and larger distance from the bar major axis than the CO maxima. The position-velocity maps show that in $\text{H}\alpha$, two velocity ‘‘plateaus’’ of emission, both upstream and downstream from the dust lane, are connected by a steep CO (and $\text{H}\alpha$) velocity gradient. Strong CO emission only exists in the region of the steep velocity gradient.

The largest velocity gradient in the CO position-velocity maps presented in Fig. 8 is about $240 \text{ km s}^{-1} \text{ arcsec}^{-1}$ in region 7. Correcting this for the inclination gives a gradient of $1.9 \text{ km s}^{-1} \text{ pc}^{-1}$. The least steep gradients further out along the bar have values around $0.5 \text{ km s}^{-1} \text{ pc}^{-1}$.

4. Discussion

4.1. Gas flow and molecular gas in the bars

4.1.1. Comparison of observations and models

Observations of NGC 7479 show dust lanes displaced toward the leading edges of the bar, accompanied by CO emission (Fig. 10) which traces dense compressed molecular material. The large velocity gradients that we see in our observations occur along these gas/dust lanes. This is consistent with the general expectation of shocks in the compressed interstellar medium. In shocks the component of velocity perpendicular to the shock has an abrupt change in magnitude. The large velocity gradients in our observations are also consistent with the models which show that gas streaming along the bar has an apogalacticon near the bar dust lanes, where the gas flow changes from having a radially outward directed velocity component to having a radially inward directed component (see, e.g., Fig. 5 in Roberts, Huntley, & van Albada 1979). The line of sight at which the bar in NGC 7479 is observed is intermediate between perpendicular and parallel to the bar, and thus favorable for seeing the large gradients in the line of sight velocity across the bar dust lanes.

Figure 9 shows position-velocity maps from observations and from a Smoothed Particle Hydrodynamics (SPH) bar flow model (Laine et al. 1998). The position-velocity slices in both the observations and the models were taken across the bar at the same distances from the nucleus, and are thus directly comparable. The model data were taken from the run with the best fitting bar pattern speed ($27 \text{ km s}^{-1} \text{ kpc}^{-1}$). The two-dimensional simulation frame was projected

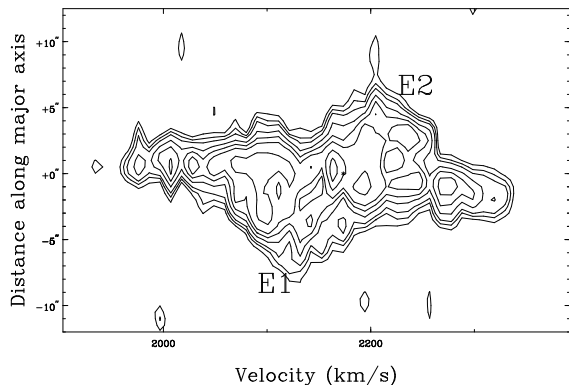


Fig. 6.— The major axis CO position–velocity plot. The contours are at 2, 3, 4, 6, 8, 10, 14, 18, 22, 24 times the rms noise in the channel maps (see Table 2). The extensions of the emission towards the south and north have been marked with E1 and E2, respectively. A possible origin of these features is discussed in the text.

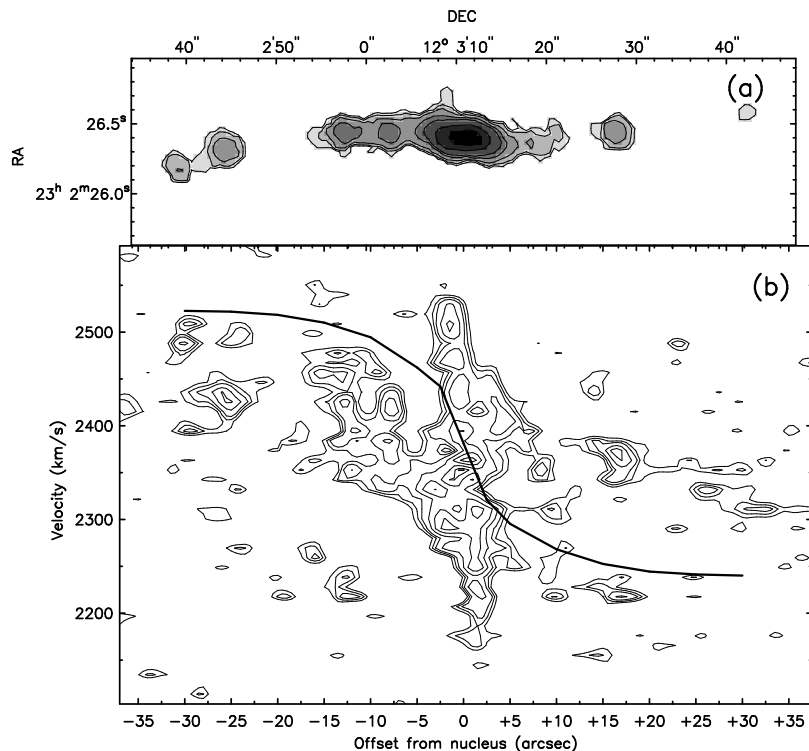


Fig. 7.— (a). The zeroth moment plot (Fig. 2). (b). The position–velocity plot along the bar at PA 177° drawn at the same scale in x-axis as (a) so that the two can be compared easily. The rotation curve derived from the gravitational potential obtained with the help of a *K*-band image (Quillen et al. 1995) has been drawn with a solid line in the position–velocity plot (after correcting it for the PA and the inclination of the plot) to show the departures from pure circular motion.

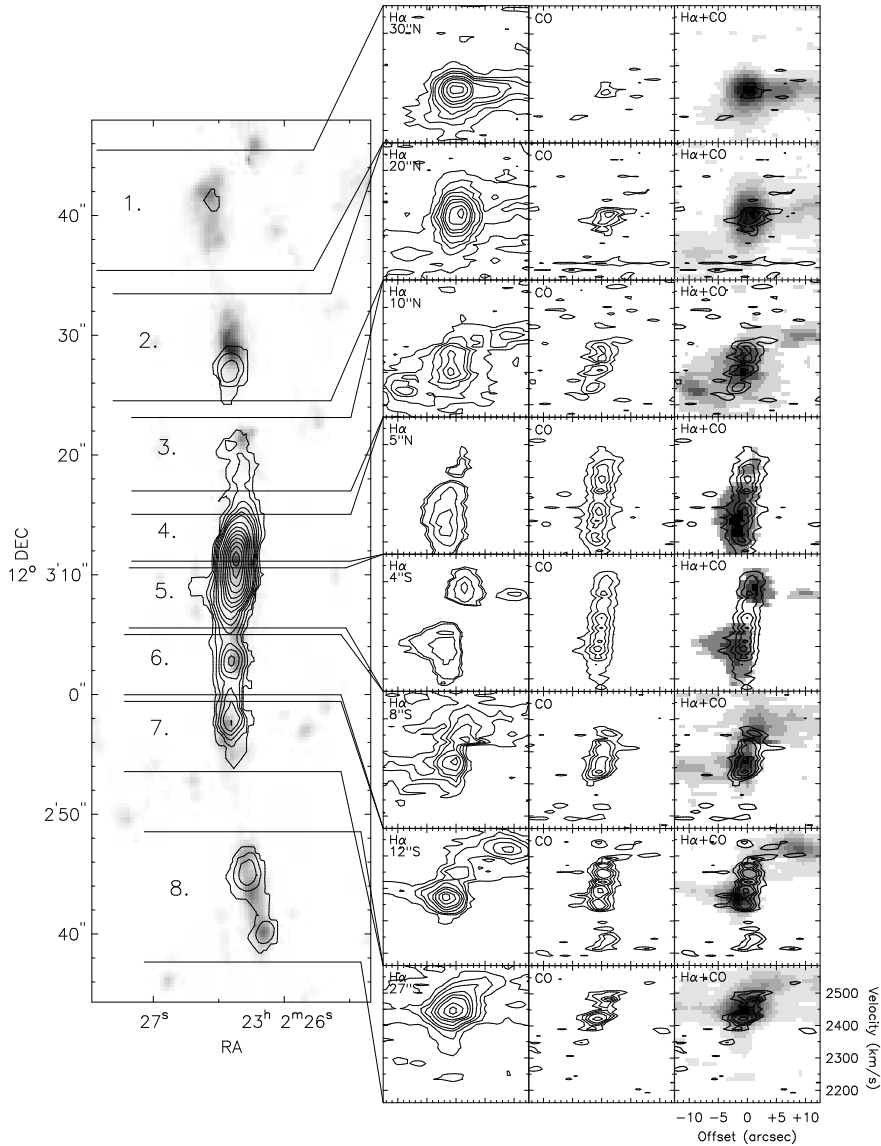


Fig. 8.— An overlay of the CO emission intensity on a gray scale image of the H α emission is shown on the left (the 0''.8 resolution H α image was kindly given to us by Dr Johan Knapen). The contours of the CO emission are given at 40, 120, 200, 280, 360, 440, 600, 760, 920, 1080, 1240, 1400, 1560, 1720 H $_2$ atoms cm $^{-2}$, using the standard conversion factor between CO intensity and H $_2$ surface density. The regions in which the emissions were integrated for the position-velocity maps are separated by solid lines, and numbered from 1 to 8. The corresponding position-velocity maps are shown on the right, the first column giving the H α maps, the second column the CO maps, and the third column both overlaid, using gray scales for the H α emission. The velocities are heliocentric. The contours on the position-velocity maps are fractions of the peak intensity in a map, chosen to give a clear presentation of the emission. The strongest CO and H α emission occurs in a narrow ridge with a large velocity gradient. Weaker H α emission is also observed both upstream and downstream from this ridge.

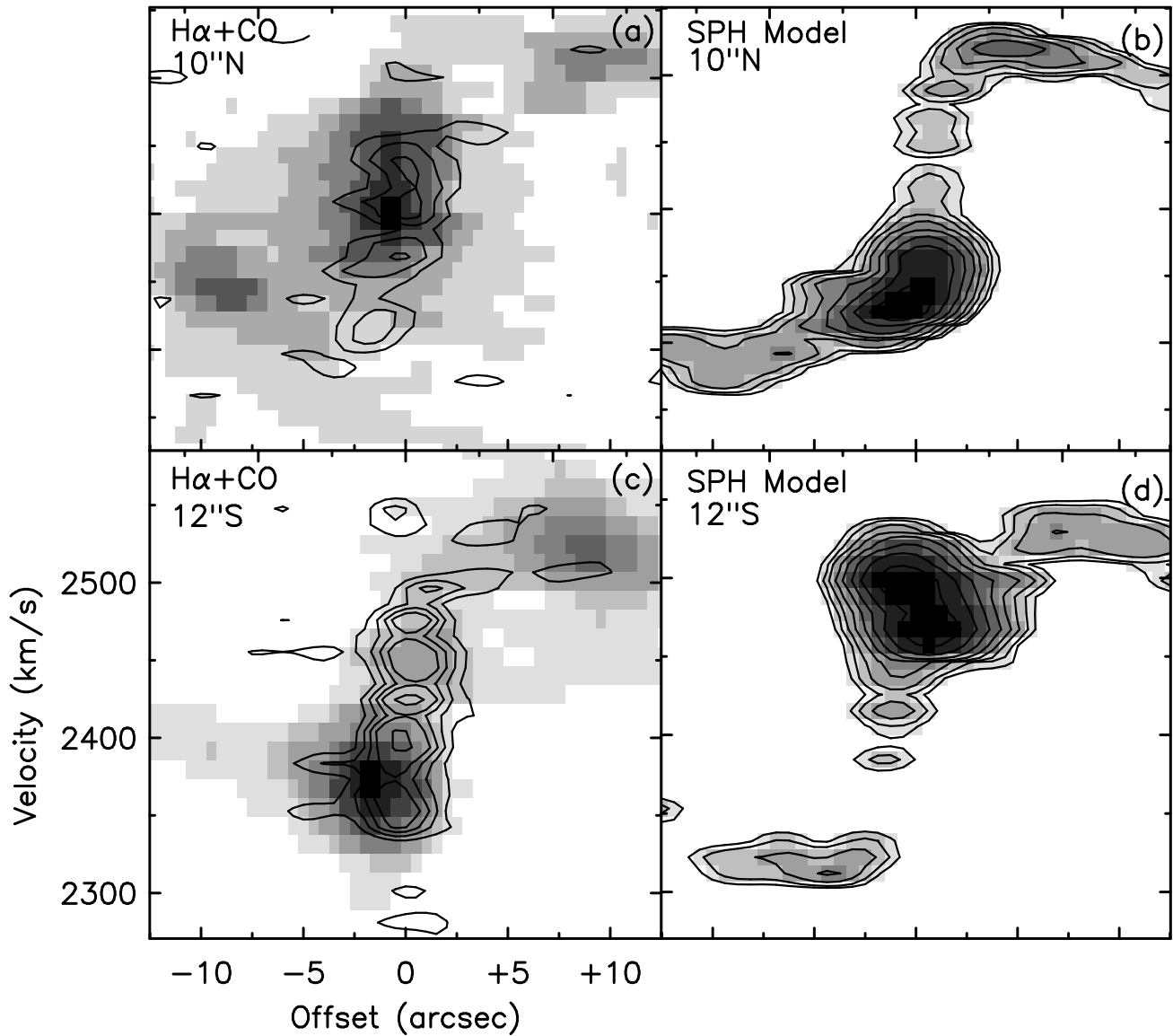


Fig. 9.— (a). Gas position–velocity maps of region 3 in Fig. 8. The H α emission is shown with gray scales and the CO emission with contours. (b). A position–velocity map of a region corresponding to (a) in the most successful model in Laine et al. (1998), at $t = 9 \times 10^8$ yr. (c). As (a), but showing region 7 in Fig. 8. (d). As (b), but corresponding to region 7 of Fig. 8. A comparison of observations and models shows that the model has succeeded in reproducing the observed morphology. Since the shock in the model takes place along the dust lane, we conclude that the observed large velocity gradients are consistent with a strong bar shock.

to the orientation of NGC 7479 (inclination 51° , PA 22° ; Laine & Gottesman 1998; the angle between the stellar bar and the kinematical major axis in the plane of the galaxy 25°). The spatial resolution of the model was smoothed by a Gaussian to $2''.5$ (400 pc) and the velocity sampled at 10.4 km s^{-1} bins, comparable to the CO (and roughly, the $\text{H}\alpha$) observations.

SPH represents total gas, and therefore it traces both the compressed regions of dust lanes and dense molecular gas as well as the more diffuse ionized gas. In both the models and the observations (Figures 7, 8, 9, 10), the observed velocity changes by about $150\text{--}200 \text{ km s}^{-1}$ across the highest gas concentrations (which in optical and near-infrared observations are seen as a dust lane; Fig. 10), but the $\text{H}\alpha$ emission “plateaus” upstream and downstream from the dust lane have relatively small velocity gradients. Our kinematical results support the expectation that the bar dust lane traces shocks in the gas flow.

The models also show the velocity “plateaus” of gas upstream and downstream from the location of the large velocity gradient. The downstream “plateaus” suggest that some fraction of the gas has moved out of the shock region. However, the mean velocity of the shock regions is consistent with radial inflow motion as mentioned in § 3.2. Therefore, apart from gas that appears to have moved downstream, away from the shock front, our observations are consistent with the picture given by Regan, Vogel, & Teuben (1997, RVT; see also Regan 1996) who claim that all gas that encounters the dust lane subsequently flows down the dust lane into the nuclear region.

Our observations and the comparison to the SPH model have shown that the response of gas (including molecular) to the forces along the bar in NGC 7479 is more consistent with the behavior of dissipative diffuse gas under hydrodynamic forces (pressure, viscosity) than the response of giant dense molecular gas clouds which might be expected to react like a ballistic particle. Both the grid-based ideal gas hydrodynamic codes and SPH codes have modeled gas flows, including the compression regions or shocks, satisfactorily in most cases. “Sticky particle” (SP) codes smear the shocks over relatively large spatial scales, depending on the particle size, and may have difficulties modelling the 100 pc scale, steep velocity gradients in the bar dust lane of NGC 7479. It is unclear at present which code is the most realistic in modeling the behavior of the interstellar medium (ISM). The equation of state of the ISM is unknown and the multiphase numerical modeling of the gas has not been done yet.

4.1.2. Properties of molecular gas in the bars

The star formation and gas flow properties along bars would be easier to understand if the physical state of the CO emitting regions was known. Specif-

ically, we would like to know if the CO emitting regions are gravitationally bound. RVT claim that the excellent agreement between their observations of NGC 1530 and the hydrodynamic models based on diffuse ideal gas suggests that the gas they traced with $\text{H}\alpha$ kinematics is diffuse gas and not concentrated in gravitationally bound giant molecular clouds (GMCs; masses up to a few times $10^6 M_\odot$) or even larger and more massive GMAs, which might behave more like ballistic particles than diffuse gas. Our observations and the comparison to models also suggests that the molecular gas in the bar of NGC 7479 does not behave like ballistic particles. In the disk of spiral galaxies the situation appears different, as complexes of GMAs have been found in at least the nearby galaxies M 51 (Rand 1993a, 1993b; Vogel, Kulkarni, & Scoville 1988), M 100 (Rand 1995), and NGC 4414 (Sakamoto 1996).

The CO luminosities (masses) and diameters of the CO emission regions along the bar in NGC 7479 are roughly similar to those seen in the *disks* of other spirals such as M 51, but the kinematics along the bar of NGC 7479 are very different. NGC 7479 has very large velocity gradients of $1.9 \text{ km s}^{-1} \text{ pc}^{-1}$ across the emitting regions. Therefore, the CO emission regions along the bar are unlikely to be self-gravitating.

The virial masses of the CO emission regions in M_\odot can be roughly estimated from

$$M_{\text{vir}} = 550D(\sigma_{1d})^2 \quad (2)$$

(Rand 1993a; Scoville & Sanders 1987). Here D is the observed FWHM diameter in parsecs, and σ_{1d} is the one-dimensional velocity dispersion in km s^{-1} . This formula assumes a $1/r$ density profile for the gas within a GMA. The mass required for the GMA to be self-gravitating is half of this mass. Using a velocity dispersion of 150 km s^{-1} and a FWHM diameter of 150 pc (about $1''$), the resulting virial mass is about $2 \times 10^9 M_\odot$. For comparison, the observed masses of the clumps along the bar (assuming the standard conversion factor) range from $9 \times 10^6 M_\odot$ to $2 \times 10^8 M_\odot$. Thus it is unlikely that the CO gas concentrations that lie along the bar are virialized or even gravitationally bound.

4.2. Star formation in the bar of NGC 7479

Star formation rates (SFRs) from the $\text{H}\alpha$ fluxes in the offset gas and dust lane along the bar have been calculated from

$$\text{SFR}_{\text{H}\alpha} = 7.07 \times 10^{-42} L(\text{H}\alpha) M_\odot \text{ yr}^{-1}, \quad (3)$$

(Bushouse 1987; see also Kennicutt 1983). Equation (3) assumes a Salpeter initial mass function (IMF) down to stars of mass $0.1 M_\odot$ and up to stars with masses of $100 M_\odot$. The $\text{H}\alpha$ fluxes have not been

corrected for extinction, so the SFRs from equation (3) are lower limits. The integrated SFR in the bar region is around $0.2 M_{\odot} \text{ yr}^{-1}$. Uncertainties due to extinction and the choice of the IMF with its cut-offs are discussed in Bushouse (1987). Specifically, Bushouse compared the global star formation rates as calculated from the $\text{H}\alpha$ fluxes (uncorrected for extinction effects) to global far-infrared fluxes. The latter were found to be three times larger on average, and therefore an average extinction correction factor of three applies to isolated galaxies. For comparison, Martin & Friedli (1997) measured the ratio of the $\text{H}\alpha$ and $\text{H}\beta$ lines in a few selected H II regions along the bar, and obtained a bar extinction value of 0.8 mag in $\text{H}\alpha$, which corresponds to a factor of 2. Multiplying the measured $\text{H}\alpha$ flux by 2.5 results in a star formation rate [SFR($\text{H}\alpha$)] of $0.5 M_{\odot} \text{ yr}^{-1}$ along the bar of NGC 7479, comparable to the value ($0.4 M_{\odot} \text{ yr}^{-1}$) obtained by Martin & Friedli (1997). The SFR for the whole galaxy, calculated from the infrared luminosity [$L(\text{IR})$; $8.9 \times 10^{10} L_{\odot}$; Young et al. 1989], is about $45 M_{\odot} \text{ yr}^{-1}$ [SFR(IR) = $1.34 \times 10^{-43} L(\text{IR})$; Hunter et al. 1986; Bushouse 1987], 90 times larger than the SFR along the bar and thus largely not seen in optical tracers, although the $\text{H}\alpha$ luminosity of the bar region is only about 10% of the total $\text{H}\alpha$ luminosity of NGC 7479.

Bushouse (1987) finds that SFR(IR) is 3–6 times larger than SFR($\text{H}\alpha$) among normal galaxies, (3 times in isolated, 6 times in interacting galaxies), most likely because of extinction in the optical. Yun & Hibbard (1998) confirmed the significantly larger SFR(IR) values and also found that the $\text{H}\alpha$ component seen in the nuclear starburst systems is dominated by the starburst superwind and scattered emission. It is possible that the nucleus of NGC 7479 hosts a starburst behind dozens of magnitudes of optical extinction. About 15% of the 21 cm continuum emission is concentrated in the central beam ($4''.3 \times 3''.85$), giving a rough size scale for the starburst region (Laine & Gottesman 1998).

The large velocity gradient of $0.5\text{--}1.9 \text{ km s}^{-1} \text{ pc}^{-1}$ across the bar dust lane of NGC 7479 is likely to be dynamically important and affect star formation. The large velocity gradient can prevent large gas concentrations within the bar dust lane from being self-gravitating, as indicated by our simple calculation in § 4.1.2.

The kinematical conditions in the bar dust lane are quite different from those in the spiral arms of M 51, which has unusually strong spiral density waves with small pitch angles. Although there is a density wave induced velocity gradient of $0.05\text{--}0.1 \text{ km s}^{-1} \text{ pc}^{-1}$ across the front half of the spiral arms of M 51 (Vogel et al. 1988; Rand 1993a), this gradient is an order of magnitude smaller than that in the bar of NGC 7479,

and is furthermore in a direction which reduces the amount of shear which otherwise occurs in a disk with a flat rotation curve.

Thus, in spiral arms the largest concentration of dense gas and the regions of reduced shear occur in the same places, and both effects increase the susceptibility of gas to gravitational collapse. In bars the largest concentration of dense gas occurs in a region of a large velocity gradient, and this opposes the susceptibility of gas to gravitational collapse.

This could be the reason why star formation is observed upstream and downstream from the dust lane as well as within it. Although the regions upstream and downstream from the shockfront have lower gas density, their smaller velocity gradients may enable star formation. As discussed in § 3, the regions upstream and downstream may have molecular gas that has a column density which is too low to be detected when averaged over the synthesized beam, but the density may be high enough to enable star formation, making it easier to understand the wide distribution of $\text{H}\alpha$ emission across the bar.

The regions with the highest gas density are regions with the largest velocity gradients. Although stars are certainly forming in this dense dust lane gas, the star formation rate may be limited by the large velocity gradients: the long timescale for star formation along the bar ($2 \times 10^9 M_{\odot} / 0.5 M_{\odot} \text{ yr}^{-1} = 4.0 \times 10^9 \text{ yr}$) implies that the bar gas is not experiencing a starburst. Again, this conclusion is subject to the effects of extinction, as discussed before, although these effects are unlikely to change the basic conclusion. Elmegreen (1979) and Kenney & Lord (1991) have also suggested that the tidal forces on the gas clouds along the bar dust lanes may inhibit star formation.

4.3. Nuclear gas mass fraction

The molecular gas mass in the centers of some spiral galaxies is a large fraction (up to at least 50%) of the total dynamical mass (Turner 1994; Kenney 1997). Under these conditions, the self-gravity of the molecular gas becomes important and may drive further inflow towards the center (Shlosman et al. 1989; Shlosman et al. 1990; Heller & Shlosman 1994; Knapen et al. 1995; Wada & Habe 1992). The gas mass fraction in the central disk of NGC 7479 can be calculated in the region that exhibits circular rotation, using the standard CO luminosity to H_2 mass conversion factor. The rotation velocity in the center is about 245 km s^{-1} . We use a radius of $1''$ for the nuclear gas disk. Using a distance of 32 Mpc, the total dynamical central mass becomes

$$M_{\text{dyn}} = \frac{rv^2}{G} = 2.2 \times 10^9 M_{\odot}. \quad (4)$$

The molecular mass in this area is $3.3 \times 10^8 M_{\odot}$ or 15% of the dynamical mass. The molecular gas mass is a considerable part of the total mass in the center, although it does not dominate the dynamics. If the rest of the mass is stellar, the average mass-to-luminosity ratio in the K -band in this central area is 0.7 in solar units. This would imply a relatively young (a few Gyrs) stellar population or alternatively a metal rich old population (Worthey 1994).

Since the star formation rate along the bar is $0.5 M_{\odot} \text{ yr}^{-1}$ and the gas inflow rate is at least $4 M_{\odot} \text{ yr}^{-1}$ (Quillen et al. 1995; Laine 1996), most of the gas presently in the bar region should reach the circumnuclear region before it turns into stars. The uncertainties are caused by the unknown amount of extinction, which may severely suppress the observed $H\alpha$ fluxes along the bar dust lane and cause an underestimate of the bar SFR. The net inflow of $2 \times 10^9 M_{\odot}$ of gas would double the nuclear mass in less than a Gyr, meaning that NGC 7479 is in a short-lived evolutionary state. The resulting increase in the nuclear mass would likely drive the evolution of the galaxy towards an earlier Hubble type (Kormendy 1993; Friedli & Benz 1993; Kenney & Jogee 1997).

5. Conclusions

The high spatial resolution CO observations of NGC 7479 together with $H\alpha$ data have shown the gas distribution and motions in a dynamically young barred spiral galaxy (cf. Kenney & Jogee 1997; Laine & Heller 1998). Our main conclusions are summarized in the following:

1. The CO emission has a strong central peak, but about 50% of the emission comes from regions outside the nuclear zone, mostly from a clumpy distribution along the bar dust lane.

2. The bar dust lane and the CO gas emission occur at the same locations within the resolution of the observations.

3. The CO velocity field is consistent with circular rotation only in the central $2''$ (300 pc) diameter region. Outside this region, the velocity field deviates strongly from pure rotation and the velocities must have a substantial (at least 100 km s^{-1}) radial component along the bar.

4. The CO emission across the bar dust lane has a large velocity gradient (up to $1.9 \text{ km s}^{-1} \text{ pc}^{-1}$) with a projected velocity change up to 200 km s^{-1} . The $H\alpha$ emission shows a similar large gradient, but it also has “plateaus” of constant velocity emission both upstream and downstream from the large velocity gradient. The large velocity gradient is consistent with combined effects of a shock and a change in the radial direction of gas streamlines in the bar dust lane.

5. The gas clumps along the bar have masses from $9 \times 10^6 M_{\odot}$ to $2 \times 10^8 M_{\odot}$ if the standard CO-to- H_2 conversion factor is assumed. However, the large velocity gradient across these complexes in the bar dust lane makes this assumption suspect.

6. No strong CO emission exists in the bar region outside the dust lane, and the gas complexes in the dust lane are unlikely to be gravitationally bound because of the large velocity gradients across them.

7. Based on the relative strengths of the CO and $H\alpha$ emissions in the nucleus and along the bar, we conclude that either the optical emission from the nucleus is strongly reduced by extinction or the star formation efficiency in the nucleus is lower than in regions along the bar.

8. The star formation timescale along the bar is long, a few Gyr. The large velocity gradients in the bar dust lane may prevent the bar gas from forming stars more rapidly.

9. Along the bar, the gas inflow rate of $4 M_{\odot} \text{ yr}^{-1}$ is much greater than the star formation rate of $0.5 M_{\odot} \text{ yr}^{-1}$, implying that most of the gas presently in the bar will reach the circumnuclear region. If that happens, within the next ~ 1 Gyr the central mass of NGC 7479 should roughly double. However, extinction in the bar dust lanes and in the nuclear region causes the cited SF rate to be a lower limit, and the actual amount of gas reaching the circumnuclear region is likely to lower.

10. The nuclear gas mass fraction is likely to be at least 15% of the total dynamical mass within the central gas disk, and therefore, the molecular gas affects the dynamics in the nuclear disk.

We are very grateful to Dr Nicholas Z. Scoville for financial support for the publication of our results and the observing run. We are grateful to Drs Michael Regan and Stuart Vogel for providing us with the $H\alpha$ data for comparison with our CO data. We thank Drs P. Martin, D. Friedli, A. Quillen, and J. Knapen for providing most of the optical and near-infrared wide-band and $H\alpha$ images used in this work. The United Kingdom Infrared Telescope is operated by the Joint Astronomy Centre on behalf of the U.K. Particle Physics and Astronomy Research Council. Some of the data reported here were obtained as part of the UKIRT Service Programme. S. L. acknowledges DSR at the University of Florida for financial support and Dr I. Shlosman for helpful discussions on bar dynamics. We thank the anonymous referee for comments that improved the paper. This work was supported in part by NSF Grant AST 93-14079.

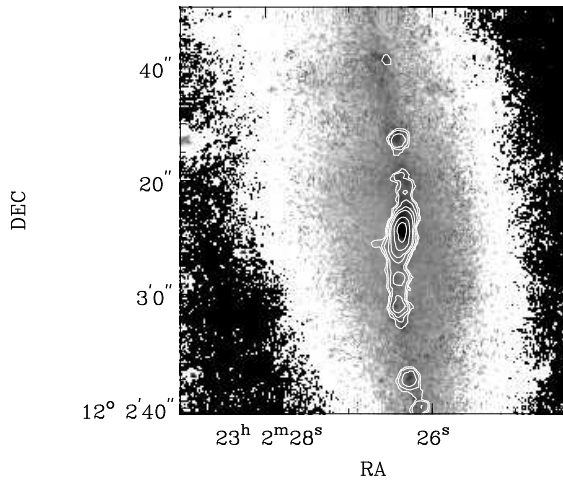


Fig. 10.— The contours of the naturally weighted CO emission overlaid on the gray scale image of a $J-K$ color map (Laine 1996), using data taken at the United Kingdom Infrared Telescope (UKIRT). Darker colors are redder regions in the gray scale map. The contour levels are at $(4, 8, 16, 32, 48, 96, 144) \times 10^{21}$ H_2 molecules cm^{-2} . The excellent spatial correlation shows that strong CO emission is associated with the high extinction in the bar dust lane.

REFERENCES

- Bloemen, J. B. G. M., et al. 1986, *A&A*, 154, 25
- Bryant, P. M., & Scoville, N. Z. 1996, *ApJ*, 457, 678
- Bushouse, H. A. 1987, *ApJ*, 320, 49
- Dahmen, G., Hüttemeister, S., Wilson, T. L., & Mauersberger, R. 1998, *A&A*, 331, 959
- Devereux, N. A. 1989, *ApJ*, 346, 126
- Elmegreen, B. G. 1979, *ApJ*, 231, 372
- Friedli, D., & Benz, W. 1993, *A&A*, 268, 65
- García-Burillo, S., Sempere, M. J., Combes, F., & Neri, R. 1998, *A&A*, 333, 864
- Heller, C. H., & Shlosman, I. 1994, *ApJ*, 424, 84
- Hunter, D. A., Gillett, F. C., Gallagher, J. S., III, Rice, W. L., & Low, F. J. 1986, *ApJ*, 303, 171
- Kenney, J. D. P. 1996, private communication
- Kenney, J. D. P. 1997, in *The Interstellar Medium in Galaxies*, ed. J. M. van der Hulst, (Dordrecht: Kluwer), 33
- Kenney, J. D. P., Carlstrom, J. E., & Young, J. S. 1993, *ApJ*, 418, 687
- Kenney, J. D. P., & Jogee, S. 1997, in *Star Formation Near and Far*, ed. S. S. Holt & L. G. Mundy (Woodbury, NY: American Institute of Physics), 247
- Kenney, J. D. P., & Lord, S. D., *ApJ*, 381, 118
- Kenney, J. D. P., & Young, J. S. 1989, *ApJ*, 344, 171
- Kennicutt, R. C., Jr. 1983, *ApJ*, 272, 54
- Knapen, J. H., Beckman, J. E., Heller, C. H., Shlosman, I., & de Jong, R. S. 1995, *ApJ*, 454, 623
- Kormendy, J. 1993, in *Galactic Bulges*, ed. H. Dejonghe & H. J. Habing, (Dordrecht: Kluwer), 209
- Laine, S. 1996, Ph.D. dissertation, University of Florida
- Laine, S., & Gottesman, S. T. 1998, *MNRAS*, 297, 1041
- Laine, S., & Heller 1998, in preparation
- Laine, S., Shlosman, I., & Heller, C. H. 1998, *MNRAS*, 297, 1052
- Lindblad, P. A. B., Lindblad P. O., & Athanassoula E. 1996, *A&A*, 313, 65
- Martin, P., & Friedli, D. 1997, *A&A*, 326, 449
- Quillen, A. C., Frogel, J. A., Kenney, J. D. P., Pogge, R. W., & DePoy, D. L. 1995, *ApJ*, 441, 549
- Rand, R. J. 1993a, *ApJ*, 404, 593
- Rand, R. J. 1993b, *ApJ*, 410, 68
- Rand, R. J. 1995, *AJ*, 109, 2444
- Regan, M. W. 1996, Ph.D. thesis, University of Maryland
- Regan, M. W., Teuben, P. J., Vogel, S. N., & van der Hulst, T. 1996, *AJ*, 112, 2549
- Regan, M. W., Vogel, S. N., & Teuben, P. J. 1997, *ApJ*, 482, L143 (RVT)
- Roberts, W. W., Jr., Huntley, J. M., & van Albada, G. D. 1979, *ApJ*, 233, 67
- Sakamoto, K. 1996, *ApJ*, 471, 173
- Scoville, N. Z., & Sanders, D. B. 1987, in *Interstellar Processes*, ed. D. Hollenbach & H. A. Thronson (Dordrecht: Reidel), 21
- Scoville, N. Z., Yun, M. S., Sanders, D. B., Clemens, D. P., & Waller, W. H. 1987, *ApJS*, 63, 821
- Shlosman, I., Begelman, M. C., & Frank, J. 1990, *Nature*, 345, 679
- Shlosman, I., Frank, J., & Begelman, M. C. 1989, *Nature*, 338, 45
- Turner, J. L. 1994, in *Mass-Transfer Induced Activity in Galaxies*, ed. I. Shlosman (Cambridge: Cambridge University Press), 90
- Vogel, S. N., Kulkarni, S. R., & Scoville, N. Z. 1988, *Nature*, 334, 402
- Vogel, S. N., Weymann, R., Rauch, M., & Hamilton, T. 1995, *ApJ*, 441, 162
- Wada, K., & Habe, A. 1992, *MNRAS*, 258, 82
- Worthey, G. 1994, *ApJS*, 95, 107
- Young, J. S., & Devereux, N. A. 1991, *ApJ*, 373, 414
- Young, J. S., Xie, S., Kenney, J. D. P., & Rice, W. L. 1989, *ApJS*, 70, 699
- Young, J. S., et al. 1995, *ApJS*, 98, 219
- Yun, M. S., & Hibbard, J. E. 1998, in preparation